DEVELOPMENT OF A 3D BIOPRINTED AIRWAY SMOOTH MUSCLE MODEL FOR MANIPULATING STRUCTURE AND MEASURING CONTRACTION

*Jeffery O Osagie[1,2], *Sanjana S Syeda[1,2], Emily Turner-Brannen[1,2], Michelle Guimond[1,2], Lumiere Parrenas[1,2], Ahsen Haroon[1,2], Philip Imasuen[1,2], Adrian R West[1,2]

* Denotes equal contributions

1, Department of Physiology and Pathophysiology, University of Manitoba, MB, Canada
2, Biology of Breathing Group, Children's Hospital Research Institute of Manitoba, MB, Canada

CORRESPONDENCE
Dr Adrian R West
Children's Hospital Research Institute of Manitoba
606A John Buhler Research Centre
715 McDermot Avenue
Winnipeg MB R3E 3P4
Canada
Email: adrian.west@umanitoba.ca
Phone: +1 204 789 3603
ORCiD: https://orcid.org/0000-0001-8079-6915

GRANTS
1. Natural Sciences and Engineering Research Council, Discovery Grant (Adrian West)
2. Research Manitoba, New Investigator Operating Grant (Adrian West)
3. Children's Hospital Research Institute of Manitoba, Operating Grant (Adrian West)
4. Canadian Foundation for Innovation, John R. Evans Leaders Fund (Adrian West)
5. University of Manitoba, Manitoba Graduate Scholarship (Jeffery Osagie)
6. Research Manitoba, Master's Studentship Award (Jeffery Osagie)
7. Research Manitoba, Master's Studentship Award (Sanjana Syeda)
8. Children's Hospital Research Institute of Manitoba, Summer Studentship (Michelle Guimond)
9. University of Manitoba, Jack Prior Memorial Undergraduate Student Research Award (Lumiere Parrenas)
10. University of Manitoba, Undergraduate Research Award (Ahsen Haroon)
11. University of Manitoba, UMSU Undergraduate Research Award (Philip Imasuen)

The grant bodies had no role in study design, data collection and analysis, decision to publish, or preparation of the manuscript.

SHORT TITLE
3D Bioprinted Airway Smooth Muscle

KEYWORDS
3D bioprinting
Airway smooth muscle
Contraction
Relaxation
Mechanobiology

ABSTRACT

The contractile function of airway smooth muscle (ASM) is inextricably linked to its mechanical properties and interaction with the surrounding mechanical environment. As tissue engineering approaches become more commonplace for studying lung biology, the inability to replicate realistic mechanical contexts for ASM will increasingly become a barrier to a fulsome understanding of lung health and disease. To address this knowledge gap, we describe the use of 3D bioprinting technology to generate a novel experimental model of ASM with a wide scope for modulating tissue mechanics.

Using a stiffness modifiable alginate-collagen-fibrinogen bioink, we demonstrate that modulating the stiffness of free-floating ASM 'bare rings' is unfeasible; bioink conditions favorable for muscle formation produce structures that rapidly collapse. However, the creation of novel 'sandwich' and 'spiderweb' designs that encapsulate the ASM bundle within stiff acellular load bearing frames successfully created variable elastic loads opposing tissue collapse and contraction. Sandwich and spiderweb constructs demonstrated realistic actin filament organisation, generated significant baseline tone, and responded appropriately to acetylcholine, potassium chloride and cytochalasin D. Importantly, the two designs feasibly simulate different mechanical contexts within the lung. Specifically, the sandwich was relatively compliant and subject to plastic deformation under high contractile loads, whereas the stiffer spiderweb was more robust and only deformed minimally after repeated maximal contractions.

Thus, our model represents a new paradigm for studying ASM contractile function in a realistic mechanical context. Moreover, it holds significant capacity to study the effects of ECM composition, multiple cell types and fibrosis on lung health and disease.

70 **INTRODUCTION**

71 Cell culture, laboratory animals, and *ex vivo* human tissue have been the foundation of biological research for
72 over 100 years. While each remains an essential scientific tool, it is becoming increasingly recognised that
73 these paradigms are not sufficient to fully understand both healthy and disease states. Biological and technical
74 issues limit the tissue- and organ-level relevance of cell culture, while ethical concerns mandate reductions in
75 the use of laboratory animals, and reliable supplies of human tissue remain scarce. Tissue engineering has
76 emerged as a compelling solution to these limitations, by promising to create a large supply of customised
77 human tissues and advanced experimental models from cultured cells to better understand basal biology and
78 to simulate human health and disease (1). In the context of the lung, many recent advancements have been
79 made with 'organ-on-a-chip' and bioreactor models that replicate the alveolar compartment, gas exchange,
80 and cell-cell interactions in the airway wall (2-6). Organoid models show extreme promise for modelling
81 different aspects of lung development and epithelial function (7-10).
82
83 Despite these advances, major deficiencies persist in our ability to engineer and study a critically important
84 lung component: airway smooth muscle (ASM). ASM composes a large portion of the airway wall by volume,
85 making it a major inflammatory mediator (11). Moreover, muscle contraction is potently modulated by the
86 mechanical environment and accurately replicating these *in vivo* environments *in vitro* has proven to be
87 challenging (12, 13). Tension development and contraction of ASM also regulate vital aspects of lung
88 physiology, and dysfunctional ASM mechanics is a central player in the pathogenesis of lung diseases such as
89 asthma (14). Key technical difficulties arise in the ability to engineer realistic mechanical environments that can
90 stand up to the rigors of muscle contraction. Early attempts successfully used simple hydrogels to measure
91 muscle contraction (15-17), although the mechanical context of these models is questionable. ASM
92 microtissues manufactured on silicone moulds (18), as well as cells on elastomeric substrates (19) and
93 electrospun scaffolds (20), have more realistically replicated many aspects of functional ASM, although short
94 lifespans in culture and narrow scope to modulate tissue mechanics remain significant limitations.
95
96 The recent description of a 3D bioprinted experimental model of ASM (21) represents a novel approach for
97 creating functional ASM tissues. In this study, a commercial bioprinter (Aspect Biosystems' RX1™) and alginate-
98 collagen bioink (AGC-10) were used to create ASM muscle rings that responded appropriately to physiological
99 contractile and relaxant signals. However, similar to early hydrogel approaches, this model does not recreate a
100 realistic mechanical environment, necessitating further development to accurately depict different
101 environments within the lung. Alginate has been used in many tissue engineering applications to modulate
102 tissue stiffness (22-25), and the RX1 bioprinter incorporates a multi-channel microfluidic printhead that could

103 feasibly deposit structural and muscle components separately, presenting several avenues for technical and
104 physiological advancement.
105
106 In the present study, we expanded on previous approaches by creating a stiffness-modifiable alginate bioink
107 and novel multi-material tissue structures. This enabled us to develop a 3D bioprinted model of ASM designed
108 specifically to interrogate the effect of tissue mechanics on muscle contraction. Critically, our approach
109 generated lifelike ASM that responded appropriately to contractile and relaxant signals and demonstrated that
110 different engineered structural properties can modulate the dynamics of ASM contraction. Finally, by testing
111 coronary artery smooth muscle (CSM) in parallel, we demonstrated that our model could be applicable to a
112 wide range of different organ contexts.

113 **METHODS**

114 **Cell Culture**

115 Senescence resistant human ASM cells (hTERT overexpression, line D12) were obtained as a generous gift from
116 the laboratory of Dr. Andrew Halayko (Department of Physiology & Pathophysiology, University of Manitoba).
117 Cells were propagated in feeder media consisting of DMEM/F12 (Gibco 11330-057) supplemented with 10%
118 heat-inactivated fetal bovine serum (Gibco 12483-020) and 1% penicillin-streptomycin (Gibco 15140-122), and
119 maintained at 37°C, 5% CO_2 and 85% humidity. To prepare for bioprinting, cells at approximately 90%
120 confluence were detached with TrypLE cell dissociation reagent (Gibco 12605-036), resuspended in a calcium-
121 free alginate diluent buffer (145 mM NaCl, 5 mM NaHCO3, pH 7.0), and gently centrifuged at 150×RCF for 5
122 minutes. The supernatant was aspirated, and cells resuspended into prepared bio-ink at a density of 2.5×10^7
123 cells/mL. Coronary Arterial Smooth Muscle cells (CSM; Applied Biological Materials T0557) were propagated
124 and prepared in the same manner, but were grown in flasks coated with rat tail collagen type I (Corning
125 354236) at 10 µg/mL in PBS.

126

127 **3D Designs**

128 Designs for 3D bioprinting and fused deposition modelling (FDM) 3D printing were created in Tinkercad
129 (https://www.tinkercad.com/) and exported as STL files (see Supplementary Files). Toolpaths for 3D bioprinting
130 were prepared from STL files in Aspect Studio software and saved as APJ files. 'Bare ring' designs were created
131 as a cylinder 8 or 10 mm in diameter and 0.6 mm high and printed with 0.04 mm layer thickness (for 15 layers),
132 0% infill, and one perimeter of cellular bioink (Fig 1A). 'Sandwich' designs encapsulated a bare ring within top
133 and bottom 13 mm diameter, 0.20 mm high cylinders as acellular layers (Fig 1B). The encapsulation layers were
134 set to a 0.04 mm layer height (for 5 layers), and 20% infill with rectilinear and concentric patterns in alternate
135 layers. 'Spiderweb' designs were created with additional mechanical supports designed to interface with a rigid
136 plastic tissue holder (Fig 1C). Briefly, tissue holders were designed with six internal posts and an outer diameter
137 set to fit securely inside a 24 mm ThinCert insert (Greiner 657638). We hand-coded bioprinter toolpaths to
138 generate a 3D design comprising a 10-layer 10 mm diameter cellular ring stacked between four layers of
139 acellular rectilinear infill from the sandwich design. This was further encapsulated by a 19 mm diameter
140 network of acellular material containing loops/voids positioned to engage with the tissue holder. Layer heights
141 were set such that the spiderweb construct was nominally 1.0 mm thick. To improve stability of constructs for
142 long-term live cell imaging, centring rings were designed to firmly hold the ThinCert inserts at the centre of a 6-
143 well microplate (Greiner 657160) without disrupting access to the basolateral chamber (see Supplementary
144 Files).

145

146 **FDM 3D Printing**

147 STL files were 3D printed using Ultimaker Cura 4 slicing software and an Ultimaker S3 3D printer (216932) fitted
148 with an AA 0.25 mm print core (200454), glass print surface (227639) and lid enclosure (Shop3D EnclosureS3).
149 Filament was stored in freshly regenerated silica gel between prints and kept within a PrintDry 2.0 filament
150 dryer at ≥65°C during printing to minimise moisture content and ensure print consistency. Tissue holders were
151 printed with Polycarbonate Transparent filament (Ultimaker 1640) using a modified version of the Cura Fine
152 (Experimental) profile (see Supplementary Files) and an adherence aid to prevent warping (Magigoo PC).
153 Printing the fine features of the tissue holder exceeded filament retraction limits, thus sacrificial cylinders were
154 interspersed between the tissue holders to consume filament and enable unlimited retractions without
155 filament damage (see Supplementary Files). Completed tissue holders were visually inspected, and those with
156 excessive stringing or obvious physical defects were discarded. Acceptable prints were washed several times
157 with distilled water then once with 70% EtOH to remove traces of the adherence aid, air dried, then passed
158 briefly through a Bunsen burner flame to remove minor surface stringing. Tissue holders were sanitized by
159 boiling in ddH_2O water for 10 minutes at full power in a 1000 W microwave oven, followed by soaking in 70%
160 EtOH under moderate vacuum for 30 minutes. They were then exposed under 70% EtOH to 400 mJ/cm^2 of UV-
161 C light per side in a Spectrolinker XL-1000 UV Crosslinker, before being transferred to a sterile field for air
162 drying and storage. ThinCert centring rings were printed with Ultrafuse PET Black filament (BASF Pet-0301a075)
163 using the Cura CPE Generic Fine profile with modifications (see Supplementary Files) and Magigoo Original
164 adherence aid. Centring rings were sanitised by the same process as for tissue holders, with the boiling step
165 omitted.

166

167 **Bioink Formulation**

168 All bioinks were comprised of alginate, collagen, and fibrinogen as appropriate to individual experiments. To
169 create stiff bioinks, we used an ultra-purified high guluronate low molecular weight alginate (NovaMatrix
170 PRONOVA SLG-20; referred to as SLG-20). Biocompatibility and soft bioinks were achieved with an RGD-
171 coupled high guluronate very low molecular weight alginate (NovaMatrix NOVATACH VLVG GRGDSP; referred
172 to as RGD-VLVG). Lyophilised alginates were diluted to working concentration of 3% w/v by adding alginate
173 diluent buffer and incubating at room temperature with gentle mixing until fully dissolved. Fibrinogen (Sigma
174 F8630-1G) was freshly prepared as a 20 mg/mL stock solution by carefully layering the powder on top of
175 alginate diluent pre-warmed to 37°C. The tube was gently swirled to mix and maintained at 37°C until fully
176 dissolved before the solution was sterilized by passing through a syringe filter (Sigma SLGV033RS), then kept on
177 ice. Collagen I was added to a pre-cooled 15 mL tube, before pre-calculated volumes of ice-cold 7.5% $NaHCO_3$,
178 1.5 M NaCl and ddH_2O were added dropwise while gently vortexing the tube to precisely neutralize the acid
179 from collagen and achieve salt concentrations of 145 mM NaCl, 5 mM $NaHCO_3$ within the final volume of the

180 completed bioink. The appropriate quantities of fibrinogen and alginate were then added dropwise with gentle
181 mixing on ice. A pH strip (5-8) was used to verify that the pH of the final mixture was in the 7.0 to 7.4 range.
182
183 **Bioprinter Setup and Printing Process**
184 An Aspect Biosystems RX1 bioprinter was set up according to the manufacturer's instructions. In brief, a DUO
185 (two bioink material channels) or QUAD (four bioink material channels) microfluidic printhead was mounted on
186 the bioprinter. Material tubes (Falcon 352096) containing bioinks and bottles containing alginate diluent buffer
187 and CAT-2 crosslinker (Aspect Biosystems 00000458) were sealed with pneumatic caps pre-threaded with
188 autoclaved PTFE microfluidic tubing (Diba Omnifit 008T16-080-20), before the material tubes were placed in an
189 ice filled tube holder. Tubing was connected to the corresponding material channels in the printhead, before
190 the system was primed to remove air and clear bubbles from the printhead and nozzle in the following order:
191 material 1 through material 4, buffer, buffer plus crosslinker, then buffer.
192
193 ThinCert inserts were pre-wetted with alginate diluent buffer and mounted on the RX1 24 mm vacuum chuck.
194 The porous membrane captured the printed material while allowing excess crosslinker and buffer to flow
195 through. Constructs were deposited layer by layer as per the specified APJ file, with pressures and speeds set
196 and constantly monitored to maintain high fidelity to the original design (Table 1 and Fig 1). All print runs were
197 completed within 30 minutes of adding cells to bio-inks to minimize variance arising from cell
198 sedimentation/clumping and premature precipitation/gelation of bioink components. For spiderweb
199 constructs, a sanitized tissue holder was manually applied immediately after printing to engage the posts with
200 loops/voids in the construct. ThinCert inserts containing the printed constructs were transferred to a 6-well
201 plate containing 4 mL of pre-warmed feeder media. Where the bioink contained fibrinogen, the feeder media
202 was supplemented with 1.25 U/mL thrombin (Sigma T4648-1KU) for 30 minutes to initiate fibrinogen cleavage
203 and polymerisation to fibrin, before constructs were switched to regular feeder media. For spiderweb designs,
204 a ThinCert Centring Ring was applied to prepare the constructs for post-print imaging (see below). Constructs
205 were maintained by changing media every two days. Prior to contraction assays, constructs were serum-
206 deprived for ≥24 hours by replacing feeder media with DMEM/F12 containing 0.5% FBS and 1% insulin-
207 transferrin-selenium (Gibco 41400-045).
208
209 **Imaging for Tissue Compaction and Contractile Function**
210 To assess compaction of bare rings and sandwich constructs, macroscopic images were captured daily using an
211 Olympus Tough TG-1 iHS digital camera mounted on a tripod. Camera height and focus were optimized using 6-
212 well plates with ThinCert inserts such that the entire plate was in the field of view. Videos of muscle responses
213 to contractile/relaxant agents and alginate decrosslinking were obtained using high-quality video mode (1080p

214 @ 30 fps). Videos were processed by ffmpegTool to create single image sequences. Spiderweb constructs were
215 imaged in a Cytation 5 MPV Cell Imaging Multimode Reader set at 37°C and 5% CO_2. Whole-well phase contrast
216 images were obtained using the montage function of the Gen5 software and a 4× lens.
217
218 **Contraction Assays**
219 To determine contractile responses of sandwich and spiderweb constructs, time-lapse images representing
220 baseline and treatment conditions were captured. Drug treatments designed to elicit maximal responses were
221 prepared in low serum media; 100 µM acetylcholine (ACh; Sigma A6625), isotonic 80 mM KCl (Sigma, 746436-
222 500) and 10 µM cytochalasin D (Cyto D; Santa Cruz, sc-201442) as described previously (18). To initiate the
223 experiment, the media on constructs was replaced by the first drug treatment, adding one-third of the dose to
224 the ThinCert apical chamber and two-thirds to the basolateral chamber, taking care not to disturb the constructs.
225 After a 10-minute exposure window, treatment images were captured, before applying the next treatment in
226 the sequence. For single maximal contraction time course experiments in spiderweb constructs, a 20-minute KCl
227 exposure was followed by a 20-minute cytochalasin D exposure, with images captured continuously at the
228 maximum capture rate.
229
230 **Alginate Depolymerization Load Removal Assay**
231 To characterize shortening dynamics of the unloaded muscle bundle and determine the relative strength of the
232 mechanical load, calcium chelation was used to rapidly de-crosslink alginate (26, 27). Baseline images were
233 taken before media was replaced with a buffer containing 40 mM tri-sodium citrate (Sigma 111037) plus 15
234 mM ethylenediaminetetraacetic acid (EDTA; Sigma E5134-50G) pH 7.2. Videos (sandwiches) and montage
235 image sequences (spiderwebs) were collected for up to 10 minutes.
236
237 **Contraction Reproducibility**
238 To determine the robustness and stability of our designs, spiderweb constructs were subjected to five successive
239 contraction/relaxation cycles. After capturing baseline images, maximal contraction was achieved by 20-minute
240 exposures to 80 mM KCl, followed by a 30-minute washout period, with images captured at peak contraction
241 and relaxation. The final washout cycle was followed by an additional treatment with 10 mM cytochalasin D to
242 ensure complete tension ablation.
243
244 **Image Processing and Calculations**
245 The lumen area of bare ring, sandwich, and spiderweb constructs was quantified with Fiji Imaging software, using
246 the manual polygon selection feature. Where suitable, the Canny Edge Detector plugin was used to highlight
247 borders to simplify and expedite measurements. Changes in lumen area were calculated as a percentage of raw

248 pixel area relative to, or delta from, post-print area (for compaction assays) and pre-contraction baselines (for
249 contraction assays).
250
251 **Histology**
252 Constructs were fixed with 4% paraformaldehyde (PFA; Sigma P6148) in Hanks Balanced Salt Solution (HBSS;
253 Gibco 14065-056) for 15 min, permeabilized with 0.1% Triton-X 100 (X-100, Sigma-Aldrich) in 4% PFA/HBSS for
254 10 min, then washed 3 times with HBSS. Filamentous actin (f-actin) was stained using 1 U per construct of Alexa
255 Fluor 488 Phalloidin (Invitrogen A12379) in HBSS for 1 hour, before washing 3 times with HBSS, and
256 counterstained with 0.1 µg/mL Hoechst 33342 (Invitrogen H1399) in HBSS for up to 20 min. Constructs were
257 washed one final time to remove unbound stain before they were transferred to a glass bottomed 12 well plate
258 (Cellvis P12-1.5H-N). One-to-two drops of SlowFade Diamond Antifade Mountant (Invitrogen S36963) were
259 added, and an 18 mm round coverslip (VWR CA48382-041) placed on top. Widefield fluorescence images were
260 captured on the Cytation 5; where necessary, images were uniformly adjusted for brightness and contrast only,
261 ensuring that no details were obscured.
262
263 **Data Analysis and Statistics**
264 All numerical data are presented as mean ± standard error. Each 'n' value represents results from a single
265 distinct bioprinted construct. Statistical tests were performed with the GraphPad Prism 6.07 software package,
266 with $p<0.05$ considered statistically significant. For all compaction time-course and contraction experiments,
267 independent samples 2-way ANOVA (factors: Stiffness, Time) was performed, with all-pairwise Tukey post-tests
268 performed for the Stiffness factor. Contractile reproducibility was assessed by independent samples 2-way
269 ANOVA (factors: Contraction/Relaxation, Cycles) with Tukey post-tests comparing contraction versus relaxation
270 within each cycle.

271 **RESULTS**

272 **Bare Ring Optimisation**

273 To begin formulating a stiffness-modifiable bioink suitable for use with ASM, we took inspiration from Aspect
274 Biosystems' previous work (21) and began producing bare ring designs containing ASM and CSM with variable
275 concentrations of SLG-20 alginate plus collagen. Rings with high concentrations of SLG-20 were mechanically
276 robust but exhibited no characteristics of functional muscle. F-actin staining revealed that cells within bare
277 rings were balled-up immediately after printing, as would be expected from the dissociation step during bioink
278 preparation (Fig 2A). However, the cells remained balled-up even after extended periods in culture (up to 7
279 days). As SLG-20 concentration was reduced to produce softer rings, or replaced in-part or completely by the
280 less-stiff RGD-VLVG, cells began to exhibit some signs of cell spreading and elongation. However, these less-stiff
281 alginate formulations resulted in rings that were extremely fragile, collapsed into a shapeless mass of tissue,
282 and began to exhibit tears in the macroscopic structure (Fig 2B).

283

284 To ensure that this phenomenon was not specific to a particular cell type, several different hTERT ASM cell
285 lines plus CSM were trialled, each with similar findings (data not shown). Increasing collagen concentration also
286 failed to improve either cell spreading or structural integrity in any alginate formulation. This created a
287 significant impasse for optimisation of bare rings; stiff bioinks that facilitated structural integrity did not
288 facilitate muscle formation/maturation, and soft bioinks that supported muscle formation were unable to
289 withstand long-term cell culture conditions due to rapid loss of structural integrity.

290

291 **Sandwich Development**

292 Several approaches were trialled to achieve a delicate balance between cell spreading and structural stability in
293 constructs made with low stiffness alginates. Initial attempts to increase internal compressive loads by
294 modifying the aspect ratio of bare rings to make them wider and flatter yielded no benefits. Printing strategies
295 were then developed to exploit the multi-material capabilities of the RX1 bioprinter, by including acellular
296 components comprised of stiff alginate, intended to provide physical support. First, a heterogenous 'Janus'
297 fibre design was trialled where cellular and acellular materials were co-deposited into a single fibre, however
298 this proved extremely challenging to print and produced muscle tissue with little functionality. Second, an
299 'alternating ring' approach interspersed stiff acellular layers within the bare ring, yielding minor but insufficient
300 structural improvements (data not shown). Finally, several methods of fully encapsulating the muscle ring
301 within an acellular structure were tested and iterated, ultimately resulting in the sandwich design (Fig 1B). The
302 intent of this design was to reduce mechanical stress/burden on the muscle bundle, allowing the cellular bioink
303 to be formulated with low alginate concentrations that facilitated tissue remodelling, and the acellular bioink
304 could be made with higher and tunable stiffnesses to provide varying loads opposing ring collapse.

305

306 An extensive iterative design process was implemented to formulate optimal cellular and acellular bioinks.
307 These were based on SLG-20, RGD-VLVG, collagen I and fibrinogen (Table 2), using a single ASM cell line (D12)
308 and CSM cells to minimise variation, with success measured by qualitative tissue/print fidelity, cell spreading,
309 actin morphology, and tissue lifespan in culture. Notably, inclusion of SLG-20 in the cellular bioink at any
310 concentration completely inhibited muscle formation, and the ideal concentration of RGD-VLVG was relatively
311 narrow. Use of collagen and fibrinogen enhanced both muscle formation and technical aspects of printing,
312 although the exact concentrations of these components did not seem to be critical. Thus, the optimal cellular
313 bioink which offered a balance between practicality and tissue formation contained 0.375% RGD-VLVG, 1.0
314 mg/mL collagen, 5.0 mg/mL fibrinogen. The optimal acellular bioink contained 0.75-1.25% SLG-20, 1.0 mg/mL
315 collagen, 5.0 mg/mL fibrinogen.

316

317 Gross morphology of constructs printed with different stiffness acellular bioinks revealed that ASM sandwiches
318 (Fig 3A-B) have modest but significant unstimulated 'compaction' of lumen area over time ($p<0.0001$),
319 indicative of baseline tone development and tissue remodelling. This effect is stiffness modulated ($p<0.0001$)
320 with 0.75% alginate constructs experiencing significantly higher compaction. Consistent with previous results,
321 ASM bare rings compacted excessively, collapsed, and rapidly became non-functional. F-actin staining for ASM
322 (Fig 3C-D) tissues printed with optimal acellular and cellular bioinks demonstrated impressive cell
323 spreading/elongation and alignment, consistent with native muscle tissue. CSM sandwiches (Fig 3E-F) followed
324 a similar dynamic over time ($p<0.0001$), but we were unable to detect statistically significant differences in
325 compaction across the stiffness range trialled ($p=0.4693$). Collectively, these results show that the sandwich
326 design successfully stabilises tissue structure and facilitates lifelike muscle morphology, establishing it as a
327 suitable platform for the assessment of contractile function.

328

329 **Sandwich Contractile Function**

330 ASM sandwich constructs responded appropriately to classic contractile stimuli (Fig 4A; $p<0.0001$), exhibiting
331 mild contractions in response to ACh and a stronger response to KCl. Cytochalasin D reduced lumen area
332 consistent with cytoskeletal tension ablation, however lumen area failed to return to baseline levels.
333 Responses were stiffness modulated ($p=0.0438$), although this modest effect was not linear, with 1.0% acellular
334 sandwiches having a weaker contractile response than 0.75 and 1.25% constructs. CSM sandwich constructs
335 exhibited similar contractile trends with apparent reductions in lumen area in response to KCl and reversal by
336 cytochalasin D, but the treatment effects were not statistically significant over time due to extremely high
337 variability between tissues (Fig 4B; $p=0.1788$). There appeared to be a trend towards linear stiffness

modulation with 1.25% acellular constructs producing the highest mean contraction and weakest mean relaxation response, but the trend was not significant (p=0.2726).

The inability of cytochalasin D to completely reverse KCl contractions and expand lumen area above baseline levels was unexpected. This result presents two possibilities: 1) ASM and CSM in our model have little-to-no baseline contractile tone, or; 2) the sandwich can prevent ring collapse during tissue maturation but is insufficient to create an elastic load that can oppose strong or rapid contractions. To ascertain the relative degree of baseline tone versus strength of the load, ASM sandwich constructs were treated with a citrate/EDTA solution to chelate calcium and depolymerise the alginate, resulting in a sudden removal of the load opposing contraction. Figure 4C shows that load removal results in significant time ($p<0.0001$) and stiffness ($p=0.0074$) linked reductions in lumen area that far exceeds the magnitude of KCl contractions. These combined data indicate that the muscle exerts a significant degree of baseline contractile tone, and that incomplete recovery of lumen area with cytochalasin D is likely due to imperfect elasticity (i.e., plastic deformation) of the acellular structure.

Spiderweb Development

To reduce plastic deformation of sandwich constructs during contraction, we further iterated on the tissue design to improve the ability of the acellular structure to behave like an elastic spring. This could not be feasibly achieved with a bioprinted acellular structure alone (data not shown). Thus, we designed a FDM 3D printed polycarbonate tissue holder to sit tightly within a ThinCert insert to create a rigid, non-compliant load against which the construct could develop tension. Six posts were precisely positioned in the holder, and hand-coded bioprinter toolpaths were created comprising circular ‘loops’ around the post positions. A constant direction of rotation, careful optimisation of loop length/width, and tight control of bioprinting speed and pressures were found to be necessary to minimise slack without closing the loops. Five layers of looping acellular structure was coded to encapsulate two layers of sandwich infill above and below the muscle bundle, which was reduced from 15 to 10 layers to balance muscle force relative to load strength and increase longevity in culture. Tissue holders were manually placed on top of the bioprinted structure immediately after printing, completing the spiderweb design and preparing the constructs for automated imaging (Fig 5A-B).

Assessment of ASM spiderweb compaction at 4 days post printing (Fig 5C) revealed similar results to the ASM sandwich. There was significant reduction in lumen area over time ($p<0.0001$) and across the stiffness range ($p=0.0036$), although somewhat surprisingly the 1.0% acellular constructs showed modestly higher compaction.

371 **Spiderweb Contractile Function**

372 Spiderweb constructs responded predictably to KCl and cytochalasin D with significant contraction and
373 relaxation phases (Fig 5D; $p<0.0001$). However, in contrast to the sandwich design, spiderweb stiffness alone
374 was unable to modulate contractile responses ($p=0.7656$), lumen area reductions to KCl were of a smaller
375 magnitude, and lumen area increases to cytochalasin D rose above baseline levels. The small magnitude of
376 spiderweb contractions relative to sandwich contractions could be attributed to reduced contractility and/or
377 increased load. To clarify this question, alginate depolymerization experiments (Fig 5E) were performed
378 revealing a strikingly rapid reduction in lumen area ($p<0.0001$) that was stiffness modulated ($p=0.0126$), with
379 0.75% acellular constructs showing the strongest response. Importantly, the contraction appeared to be
380 considerably faster and more extensive than observed for sandwich constructs (Fig 4C). This suggests that the
381 spiderweb muscle exerts a high degree of baseline contractile tone, and that the acellular load provides
382 significant elasticity to oppose this force.

383

384 The dynamics of tension development in spiderweb designs was assessed by exposing a 0.75% acellular
385 construct to KCl and cytochalasin D for 20 minutes each (Fig 6A). The contraction phase resulted in a steady
386 reduction in lumen area that did not fully peak after 20 minutes. Cytochalasin D application resulted in a rapid
387 and extensive reversal of contraction with lumen area ending up larger than baseline levels, indicating the
388 spiderweb successfully generated a more effective spring than the sandwich.

389

390 During repeat contraction/washout cycles, lumen areas of 0.75% acellular spiderweb constructs progressively
391 decreased (Fig 6B). Analysis of each cycle (Fig 6C) revealed that the magnitude of contraction during the first
392 cycle was significantly larger than subsequent cycles ($p=0.0314$), and that contraction was significantly larger
393 than washout relaxation across the experimental time course ($p=0.0005$). A final treatment with cytochalasin D
394 after the last cycle resulted in significant additional relaxation, indicating a progressive increase in baseline
395 muscle tone. Since cytochalasin D could not fully return lumen area to baseline levels, this suggests that the
396 spiderweb construct is still subject to plastic deformation when exposed to excessive contractile force.

397 **DISCUSSION**

398 Creating physiologically relevant smooth muscle suitable for evaluating contraction remains a significant
399 challenge for tissue engineering. This is particularly important within the context of the lung, where structure,
400 function, and forces generated by ASM are inextricably linked. The recent description of a novel bioprinted
401 experimental model of ASM (21) raises intriguing possibilities to create customised tissues that replicate
402 different mechanical environments associated with development, health, and disease. In this study, we
403 describe the development of innovative multi-material tissue designs that were enabled by the RX1
404 bioprinter's ability to seamlessly switch between cellular and acellular bioinks within a single tissue engineered
405 construct. Combined with a stiffness-tunable alginate-collagen-fibrinogen bioink, this allowed us to create
406 widely different mechanical contexts for tissue engineered ASM. Importantly, we demonstrate that changes in
407 the mechanical environment significantly modulate ASM contractile function.

408

409 **Structural Modulation of Tissue Engineered Muscle**

410 Our study demonstrates the potent ability of tissue structure to drive a wide range of muscle function from the
411 same cells and bioink components. Importantly, we highlight the pitfalls of not considering mechanical factors
412 when engineering lung tissues that include a muscle component. Bare rings that represent muscle with an
413 inappropriate mechanical load opposing contraction rapidly collapse and become non-contractile, even as cell
414 viability and cellular morphology may remain qualitatively acceptable. Muscle formed in this manner may meet
415 many metrics of experimental success but has no *in situ* physiological equivalent and would likely provide
416 artifactual results for any experiment relating to contractile function.

417

418 The encapsulated sandwich and spiderweb designs represent a physiologically relevant mechanical load, and
419 direct parallels can be drawn to the structure and function of different lung tissues. The mild mechanical load
420 and resulting contractile dynamics offered by the sandwich design could be considered equivalent to a small
421 non-cartilaginous airway. In this context, the mild load allows a relatively high degree of muscle shortening
422 during contraction, and contraction/relaxation plastic deformation of the structure may simulate airway
423 closure. Further, the relatively slow rate of shortening observed when the mechanical load is removed by
424 depolymerising alginate with citrate/EDTA is comparable to the relatively low baseline tone seen in small
425 airway smooth muscle. In contrast, the more robust load provided by the spiderweb design appears more akin
426 to large cartilaginous airways. The magnitude of muscle shortening during KCl contractions is restricted by the
427 load, and the rapid shortening upon load removal is strikingly similar to the shortening that occurs during
428 dissection of highly tonic tracheal smooth muscle.

429

430 Within each tissue design, stiffness modulation of the structural component produced somewhat inconsistent
431 results. The predicted weaker loads produced by the 0.75% acellular bioink allow greater sandwich compaction
432 during ASM tissue formation, yet spiderweb compaction was significantly greater in 1.0% acellular ASM
433 constructs, and no statistically significant difference was observed in CSM. Load removal experiments exhibited
434 more consistency; in both sandwich and spiderweb tissues, 0.75% acellular constructs exhibited faster and
435 more extensive shortening during load removal, as expected from the reduced quantity/density of alginate
436 that needs to depolymerise. Contractile responses were also diverse in the different tissues and structures
437 trialled; ASM sandwiches had the smallest contraction in 1.0% acellular tissues, CSM sandwiches trended
438 towards larger contractions with increasing stiffness, and ASM spiderwebs contracted similarly irrespective of
439 acellular stiffness. A key confounding factor that possibly contributed to inconsistencies in contractile function
440 is that our results were normalised to a baseline lumen area recorded immediately prior to contraction
441 experiments. This is directly equivalent to standard protocols that set baseline length (28) or optimal passive
442 force (29) prior to *ex vivo* smooth muscle strip experiments. However, adopting this approach in our model
443 masks the effect of varying levels of muscle maturation and tissue compaction preceding evaluation of
444 contractile responses, which may represent different degrees of tissue remodelling versus baseline tone
445 development. Moving forward, it will be essential to image every construct immediately after printing and
446 before contraction experiments to account for this variable.
447
448 It is also possible that the effects of differing acellular load stiffness are below the sensitivity of instruments
449 used to capture contractile responses. Lumen area changes in spiderwebs are notably small and may be subject
450 to noise despite our rigorous imaging and measurement protocols. We expect that clearer patterns would
451 emerge with a wider range of acellular stiffnesses within each tissue design. In this study we used acellular SLG-
452 20 alginate concentrations from 0.75% to 1.25%, representing the lowest and highest bioink viscosities
453 printable with high fidelity and near-perfect reliability. Based on printing pressures (Table 1) this range covers
454 an approximate doubling of bioink viscosity and resultant fibre stiffness. However, to better highlight stiffness
455 modulation of contraction, an expanded concentration range of 0.5 to 1.5% SLG-20 is entirely feasible (albeit
456 with a lower success rate of producing high fidelity constructs) and would be expected to produce more than a
457 three-fold difference in fibre stiffness between the softest and stiffest constructs. Finally, this foundational
458 design study primarily considers muscle function in terms of physical shortening, which is a relatively narrow
459 view of the many potential factors modulated by tissue mechanics. Future studies will examine other
460 experimental outcomes with a wider dynamic range of measurements including contractile vs synthetic
461 phenotype, calcium handling, proliferation, and ECM remodelling.
462

463 **Contrasts to Other Tissue Engineering Approaches**

464 The bare ring, sandwich, and spiderweb designs developed in this study offer striking similarities and disparities
465 to comparable hydrogel models of tissue engineered ASM. Notably, a foundational 3D bioprinting paper by
466 Dickman *et al* used an alginate-collagen bioink (AGC-10) to create primary human ASM muscle rings that
467 compacted without collapsing [see Ref (21) Fig 2]. Our inability to replicate similar data may be related to
468 distinct properties of AGC-10, or attributable to use of ASM cells with significantly different mechanical and
469 contractile properties. Indeed, discussions with the authors revealed that muscle rings made with some ASM
470 cell samples did collapse, and these tissues were excluded from their experiments. Wide variation in primary
471 ASM cell samples is normal and expected, but such an approach may bias cell selection towards low-contractile
472 cells incapable of generating high amounts of force. This highlights a key benefit of our designs; the acellular
473 layers generate a significant load opposing cellular tension, allowing both weakly and highly contractile cells to
474 be used in identical conditions without fear of collapse.
475
476 The ASM microtissue model (18) provides an excellent point of comparison since the studies used the same
477 ASM cell line and key contractile experiments were performed with similar protocols. Indeed, several
478 physiological aspects of the sandwich and spiderweb constructs were remarkably similar to microtissues,
479 including actin morphology, the relative magnitude of ACh and KCl contractions, and time courses for maximal
480 contraction and relaxation. Yet, a marked point of difference between the microtissue model and this study lies
481 in the dynamics of multiple contraction and washout relaxation cycles in spiderweb constructs [see Ref (18) Fig
482 4E]. In both experimental models the first contraction was greater than subsequent contractions, but in
483 spiderweb designs each contraction was of greater magnitude than the subsequent washout relaxation,
484 resulting in a progressive decrease in lumen area with each cycle. The incomplete relaxation after the final
485 cytochalasin D treatment indicates that this phenomenon derives in-part from plastic deformation of the
486 spiderweb throughout the experiment. However, the large magnitude of cytochalasin D relaxation suggests
487 that the washout step alone is incapable of fully relaxing the muscle, and that active actinomyosin crossbridge
488 cycling and/or passive cytoskeletal tension accumulates with successive contractions.
489
490 The reason for this contrasting relaxation response is unclear, although key technical differences between the
491 models may contribute. Spiderweb muscle bundles are significantly larger than microtissues with a greater
492 diffusion barrier that potentially increases washout times. However, single-contraction time courses were
493 highly comparable between the models indicating this is not a major factor. The inclusion of supporting
494 fibroblasts in ASM microtissues is noteworthy, although it seems doubtful that fibroblasts would modulate
495 muscle relaxation in this manner. More likely, limitations on microtissue lifespan mean they were cultured for
496 shorter time periods than spiderwebs (typically 3 days versus 5 days) and had less exposure to low serum

497 media (2 hours versus ≥24 hours), each of which may significantly modulate muscle relaxation. Finally, the
498 silicone cantilevers of the microtissue model behave like perfect springs, with virtually no hysteresis nor plastic
499 deformation, which may actively pull on the tissues to facilitate lengthening during relaxation versus the less
500 elastic spiderweb design. Examining other features relating to relaxation, including the use of alternative
501 relaxant agents (β_2 agonists, adenylate cyclase activators, rho kinase inhibitors), tracking cytoplasmic calcium,
502 and characterising cytoskeletal morphology will be essential to develop a complete understanding of this
503 differential relaxation behaviour.
504
505 In terms of practicalities, our bioprinted designs offer significant benefits over microtissues and other models
506 based on deformable silicone moulds. All aspects of the sandwich and spiderweb designs are far easier and less
507 resource intensive to produce than microtissue and other silicone substrates, tissue mechanical properties can
508 be altered 'on the fly' without changing silicone manufacturing processes, and the entire bioprinting process
509 requires only off-the-shelf equipment and reagents. The bioprinting process can be completed by a moderately
510 skilled operator and does not require laborious and highly skilled preparation of substrates including degassing
511 of wells, centrifugation, or substrate 'scraping' steps. Importantly, bioprinting may be more suitable to obtain
512 reliable results from rare or expensive cell samples. While large quantities of cells are required for each
513 bioprinting run ($\geq 5\times10^6$ cells), virtually all of the cells can be incorporated into constructs. Only 1×10^6 cells are
514 required for manufacturing microtissues, but it is estimated that less than 5×10^4 cells end up within constructs
515 due to manufacturing losses associated with centrifugation and scraping. Finally, bioprinted tissues last
516 significantly longer in culture than microtissues and automated measurement protocols are easier to establish,
517 making them suitable for a much wider range of experiments.
518
519 **Other Limitations and Opportunities for Deconstructing the Lung**
520 The narrow range of alginate types and concentrations that generated functional smooth muscle tissue was
521 surprising. We had initially expected to create a bioink based on RGD-VLVG where muscle bundle stiffness
522 could be widely modulated by addition of stiffer alginates. However, alginate content needed to be kept
523 relatively low, and inclusion of higher molecular weight alginates – even at concentrations as a low as 0.1% –
524 completely inhibited tissue formation. This may be consistent with previous studies that show high native
525 alginate concentrations impact cell function due to poor diffusivity and porosity (22, 23), and that alginate
526 chain length specifically regulates cell spreading (25). In this context, a bioink comprised of ultra low molecular
527 weight alginate generated by alginate lyase treatment (24) may provide greater scope for modulating the
528 stiffness of the muscle bundle, since alginate concentration could likely be increased without inhibiting cell
529 spreading. This approach was not pursued in this study; the ability of the sandwich and spiderweb designs to
530 completely uncouple the cellular and acellular components provided significant freedom for construct

531 optimisation. Nevertheless, the inability to use alginate to stiffen the muscle bundle may reduce the capacity to
532 simulate some aspects of fibrosis, and alternative approaches such as matrix crosslinking (30, 31), inclusion of
533 fibroblasts (18), or treatment with mediators of fibrosis (21) may be more fruitful.
534
535 In contrast to the rigid limits on alginate composition, the wide range of ECM protein content achievable within
536 the bioinks was impressive. Inclusion of small amounts of collagen I significantly improved structural integrity
537 immediately after printing, likely due to collagen thermal gelling contributing to layer adhesion. Collagen I also
538 improved tissue formation versus RGD-alginate alone, consistent with its well-known role for improving
539 biocompatibility in cell culture and tissue engineering applications. Fibrinogen inclusion (with post-print
540 conversion to fibrin) was not inherently required to create contractile ASM, but was beneficial for improving
541 long-term structural integrity of constructs. This is expected from the excellent mechanical properties of
542 fibrin/collagen co-gels (32), the resistance of fibrin to degradation by proteases normally secreted by smooth
543 muscle (33-35), and the absence of plasminogen in our culture system. Intriguingly, the upper limit of collagen
544 and fibrinogen concentrations was restricted only by practicalities of stock solution concentrations and the
545 quantity that could be physically mixed into the bioink while still maintaining osmolarity and pH. This raises the
546 possibility that collagen and fibrinogen could be, in-part or completely, substituted by alternate ECM proteins
547 including decellularized ECM (36, 37) to test the effects of different ECM milieu on muscle function. Usage of
548 dECM may be particularly beneficial, as the inclusion of dECM in bioprinted intestinal smooth muscle
549 constructs was shown to improve contractile function (21). Moreover, the nature of the sandwich and
550 spiderweb designs mean that these ECM substitutions can be made freely without concern for interfering with
551 muscle loading, creating a powerful tool to study how ECM derangement interacts with tissue mechanics.
552
553 **Summary**
554 We have developed a physiologically relevant bioprinted model of ASM that enables extensive manipulation of
555 tissue mechanics. The combination of a stiffness-tunable bioink, partnered with a microfluidic-based multi-
556 material bioprinter than enables the novel sandwich and spiderweb designs, allows us to interrogate the effect
557 of lung structure on ASM contraction more readily than any other tissue engineered model. Future studies
558 examining a broader range of stiffness environments, alternative ECM components, and simulated fibrosis by
559 including fibroblasts or through ECM crosslinking, will provide valuable insights into lung development, health,
560 and disease.

561 **SUPPLEMENTARY FILES**

562 Supplementary files are available as a private link for review at https://figshare.com/s/a36437e31e92fbb4fb7e
563 The linked zip file contains:
564 Bare Ring.STL (STL file for 10 mm bare rings)
565 Sandwich.STL (STL file for sandwich design with 13 mm frame and 10 mm muscle ring)
566 Tissue Holder Thincert v4 22.8.STL (STL file for spiderweb tissue holder)
567 Tissue Holder Retraction Count Buster.STL (STL file for sacrificial filament usage)
568 UM PC for Tissue Holder.CURAPROFILE (printing profile for spiderweb tissue holder)
569 UMS3_Tissue Holder Thincert v4 22.8 (Cura 4 Project file for tissue holder for Ultimaker S3)
570 Thincert Centring Holder v3.STL (STL file for Thincert centring ring)
571 BASF Ultrafuse PET for Centring Holder.CURAPROFILE (printing profile for Thincert Centring Ring)
572 UMS3_Thincert Centring Holder v3 (Cura 4 Project file for Thincert centring ring)
573

574 **ACKNOWLEDGEMENTS**

575 The authors would like to thank Samuel Wadsworth, Erin Bedford and Simon Beyer from Aspect Biosystems for
576 helpful discussions and technical support relating to bioink design strategies, 3D design, and hand-coding
577 bioprinter toolpaths. We thank Dr Andrew Halayko (Department of Physiology & Pathophysiology, University of
578 Manitoba) for supplying the D12 ASM cell line.
579

580 **AUTHOR CONTRIBUTIONS**

581 Jeffery Osagie edited the manuscript, designed experiments, and performed data/statistical analysis, cell
582 culture and contraction assays
583 Sanjana Syeda edited the manuscript, designed experiments, and performed data/statistical analysis, cell
584 culture and contraction assays
585 Emily Turner-Brannen edited the manuscript, analysed data, and performed bioprinting, cell culture and
586 contraction assays
587 Michelle Guimond performed 3D FDM design
588 Lumiere Parrenas tested 3D FDM designs, and performed cell culture and contraction assays
589 Ahsen Haroon tested 3D FDM designs, and performed cell culture and contraction assays
590 Philip Imasuen tested 3D FDM designs, and performed cell culture and contraction assays
591 Adrian R West conceived the study, wrote the manuscript, designed/supervised all aspects of experimentation,
592 and performed data/statistical analysis, 3D design, FDM 3D printing and bioprinting

593 **TABLES**

594 **Table 1.**

595 Print pressures and speeds for select bioink formulations during bare ring and sandwich/spiderweb
596 optimisation and experimentation phases. Pressures were qualitatively monitored during printing to maintain
597 fidelity to the original 3D design and comparable deposition rates between different bioink viscosities.

598

Bare ring optimisation	**Print Pressure (mBar)**	**Print Speed (mm/sec)**
Cellular 0.25% RGD-VLVG	18-22	32
Cellular 0.375% RGD-VLVG	20-28	32
Cellular 0.5% RGD-VLVG	25-30	32
Cellular 0.75% RGD-VLVG	30-50	30
Cellular 0.75% SLG20	55-60	23
Cellular 1.0% SLG20	80-100	20
Optimised for sandwiches and spiderwebs	**Print Pressure (mBar)**	**Print Speed (mm/sec)**
Cellular, 0.375% RGD-VLVG	25-35	32
Acellular, 0.75% SLG20	80-100	23
Acellular, 1.0% SLG20	120-150	20
Acellular, 1.25% SLG20	160-200	18
Crosslinker	60-70	N/A
Buffer	100	N/A

599

600 **Table 2.**

601 Summary of bioink components and their usable concentration range within cellular (muscle) and acellular
602 (structural) components of 3D bioprinted sandwich and spiderweb constructs. For convenience, the acellular
603 bioink was typically made with the same collagen and fibrinogen content as the cellular bioink.

604

Cellular bioink component	**Optimal concentration (usable range)**	**Effect of lower than optimal concentrations**	**Effect of higher than optimal concentrations**
SLG20	<0.1%	N/A	Prevention of cell-cell contacts
RGD-VLVG	0.375% (0.25-0.50)	Poor morphology	Reduction of cell-cell contacts
Collagen I	1.0 mg/mL (0.5-2.0)	Unravelling of constructs immediately after printing	No benefit
Fibrinogen	5.0 mg/mL (1.0-20)	Reduced structural integrity, reduction of cell-cell contacts	No benefit
Acellular bioink component	**Optimal concentration (usable range)**	**Effect of lower than optimal concentrations**	**Effect of higher than optimal concentrations**
SLG20	0.75-1.25% (0.5-1.5%)	Low viscosity, decreased print fidelity, high print speeds	High viscosity, decreased print fidelity, low print speeds
RGD-VLVG	Not used	N/A	N/A
Collagen I	1.0 mg/mL (0.5-2.0)	Unravelling of constructs immediately after printing	No benefit
Fibrinogen	5.0 mg/mL (1.0-20)	Reduced structural integrity	Increased acellular stiffness

605

606 **FIGURES**

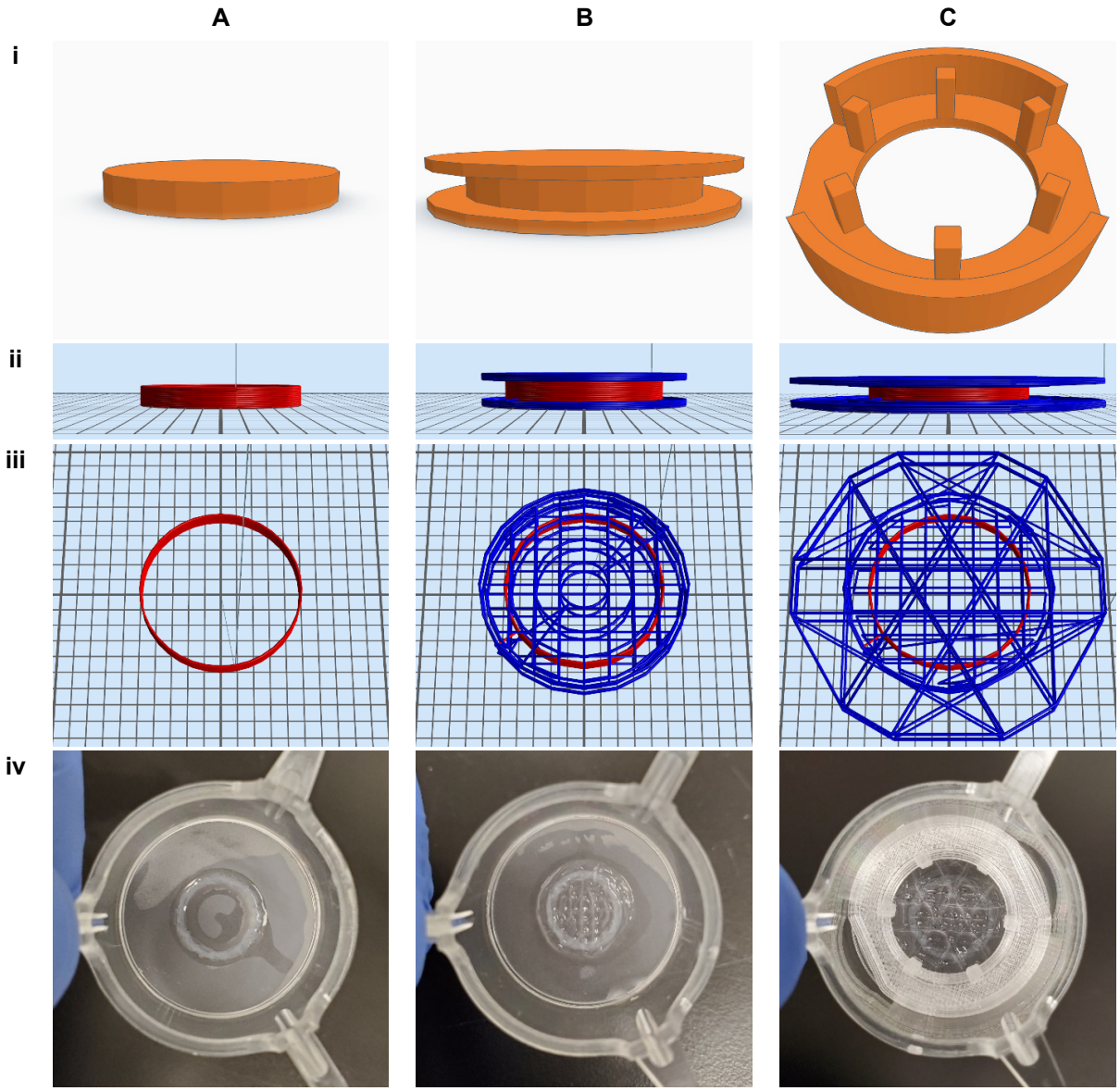

607 **Figure 1. 3D STL designs and toolpaths for bioprinting and FDM printing.**
608 Schematic of bare rings (A), sandwich (B), and spiderweb (C) designs showing STL files (i), bioprinter toolpaths
609 (ii and iii) and photos of freshly printed constructs (iv). Bare rings consisted of a 10 mm diameter cylinder
610 printed with cellular bioink (red) in a single circumference 15 layers high. The sandwich design encapsulated
611 the bare cellular ring between two 13 mm dimeter cylinders, with alternating rectilinear and circular infill
612 patterns of acellular bioink (blue) creating a spring-like load opposing tissue compaction and contraction. The
613 spiderweb design began as a solid tissue holder; the posts were designed to engage with voids in a hand-coded
614 toolpath for acellular bioink that further encapsulated and supported the cellular ring. Each of the three are
615 printed with very high fidelity to the base design. The Z-height of ring and sandwich STL files, plus all toolpaths,
616 are scaled to 200% for visual clarity.

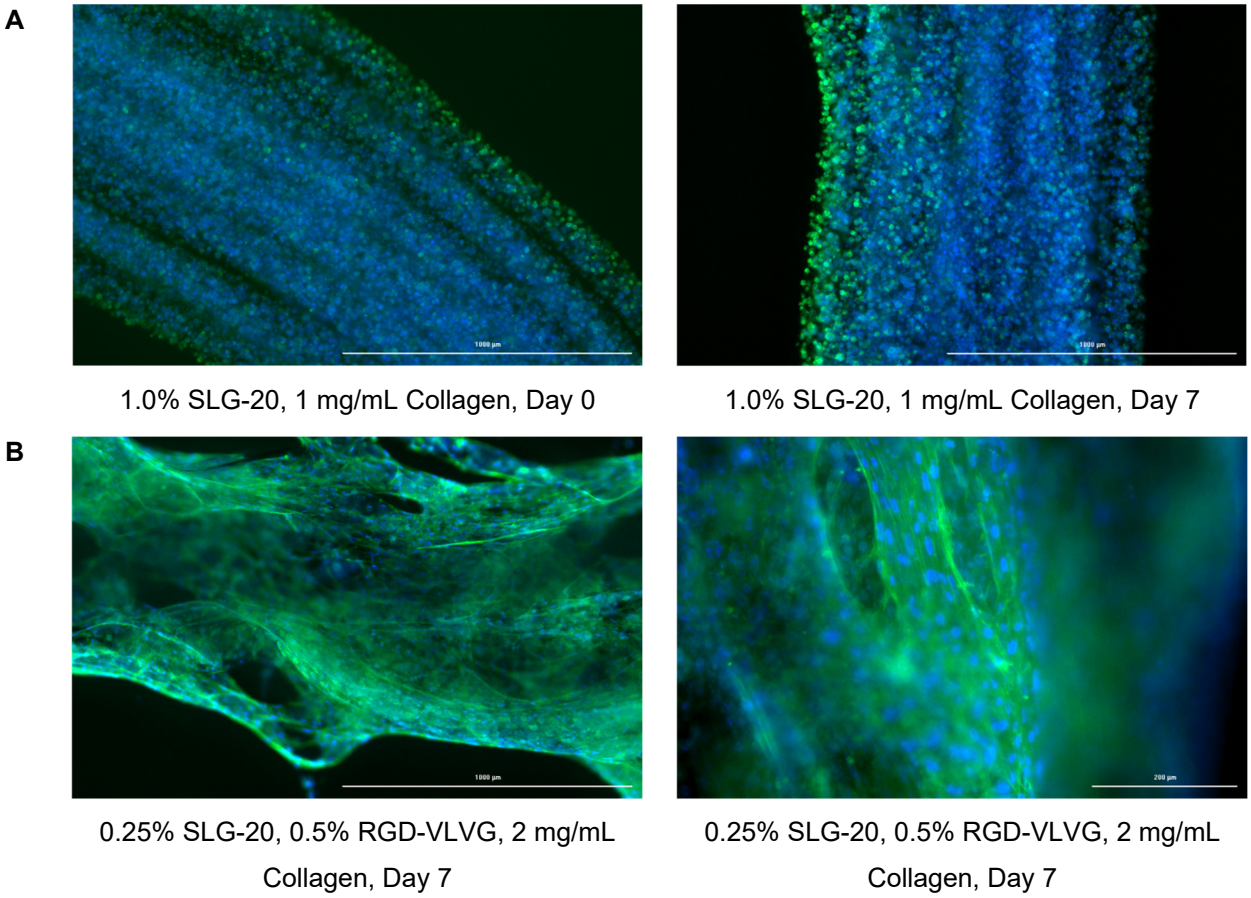

Figure 2. Histology of bare ASM rings with different bioink formulations.

Bare rings formulated with high concentrations of SLG-20 produced high fidelity and robust structures (A), however cells did not form functional muscle due to an absence of cell spreading, as evidenced by disorganised f-actin (green) and nuclei (blue) staining even after extended culture periods. Lower concentrations of SLG-20 and substitution of SLG-20 with RGD-VLVG allowed cells to spread within the construct (B). However, the macroscopic structure began to show tears in the fibre and collapses soon after printing. These results were consistent regardless of cell line/type and collagen concentration.

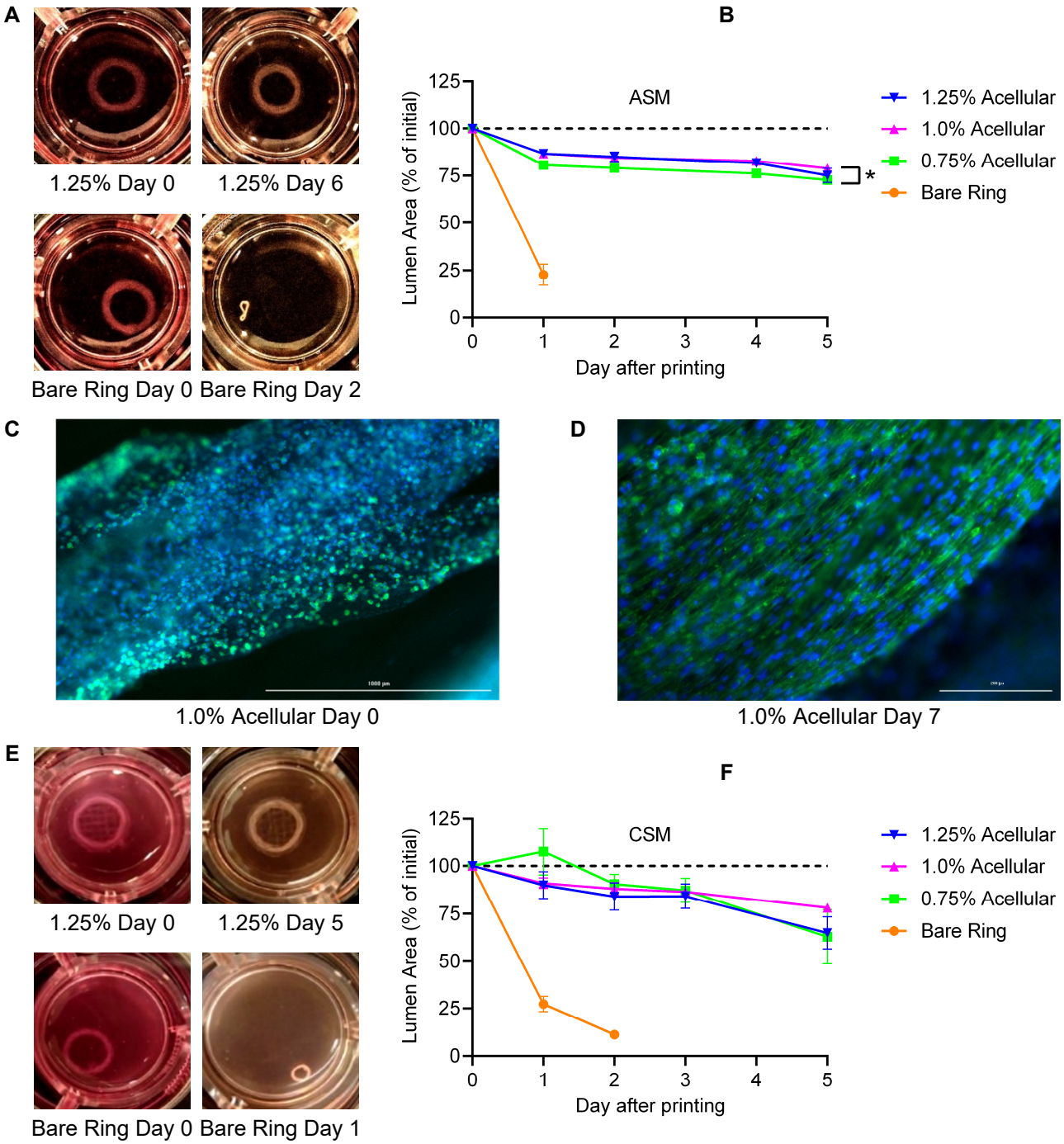

Figure 3. The sandwich design opposes muscle ring collapse and promotes muscle-like morphology. ASM sandwiches are qualitatively equivalent to bare rings immediately after printing, but the sandwich structure effectively prevents ring collapse (A). Compaction of ASM sandwiches is moderately but significantly regulated by times and acellular stiffness (B; interaction p=0.5164, time p<0.0001, stiffness p<0.0001, n=12). Widefield fluorescence of ASM sandwiches for f-actin (green) and nuclei (blue) reveals disorganised and rounded cells immediately after printing (C), but cells rapidly take on an elongated morphology with f-actin alignment along the length of the muscle bundle which is highly reminiscent of real muscle (D). CSM

633 sandwiches are similarly resistant to collapse over extended culture periods (E); they exhibit a highly similar
634 time-based compaction, although this is not modulated by acellular stiffness (F; interaction $p=0.5949$, time
635 $p<0.0001$, stiffness $p=0.4693$, $n=4$). Note that bare rings are shown on graphs for reference but are excluded
636 from statistical analysis. * represents a significant stiffness effect.

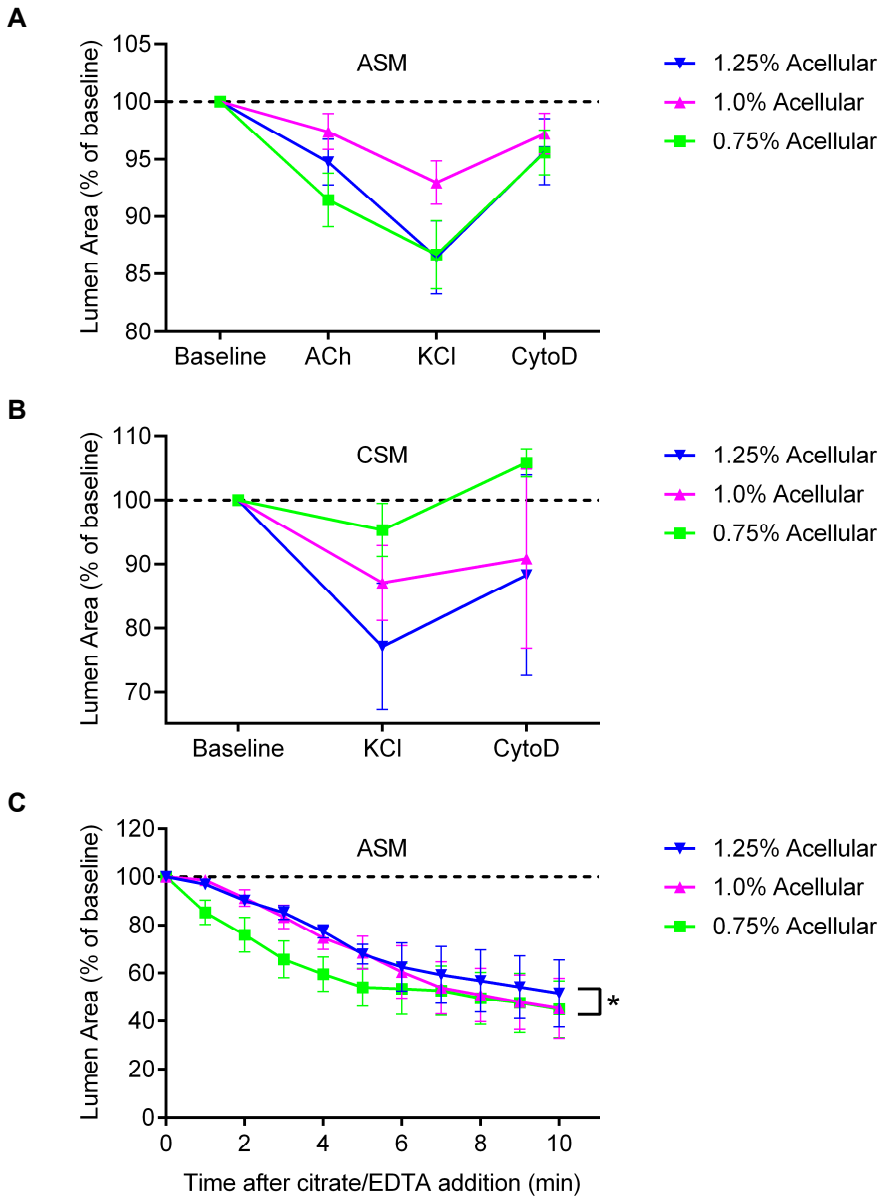

Figure 4. Contraction and relaxation of ASM and CSM sandwich designs.

ASM sandwich constructs exhibit a drug- and stiffness-dependent contractile response (A; interaction $p=0.5524$, drug $p<0.0001$, stiffness $p=0.0438$, $n=10$), with mild contraction responses to acetylcholine, a stronger response to KCl, but only partial reversal of contraction by cytochalasin D. Surprisingly, the 1.0% acellular constructs exhibited significantly weaker response, despite being the median of the stiffness range. CSM also appeared to have similar contractile responses, but no significant differences were detectable due to high variation between samples (B; interaction $p=0.8110$, drug $p=0.1788$, stiffness $p=0.2726$, $n\geq4$). Chelation-depolymerization of the alginate load in ASM sandwich constructs resulted in time- and stiffness-dependent reductions in lumen area (C; interaction $p=0.9981$, time $p<0.0001$, stiffness $p<0.0074$, $n\geq2$), indicating that the muscle has substantial baseline tone, and that contraction can cause plastic deformation of the sandwich. * represents a significant stiffness effect.

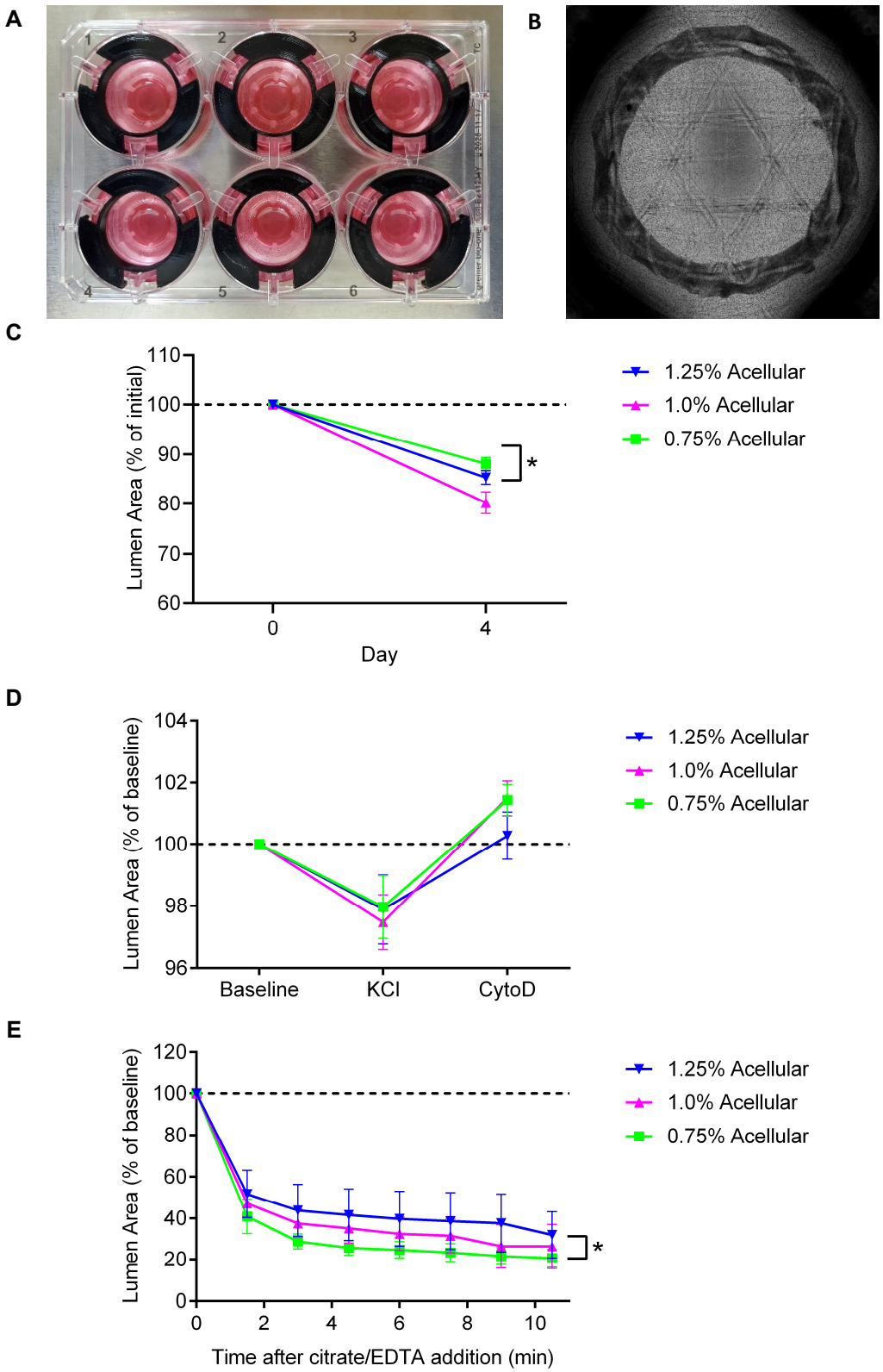

Figure 5. The spiderweb design presents a strong and elastic load opposing ASM contraction. The ASM ring within spiderweb designs is fixed in place by ThinCert centring rings, the tissue holder, and the taut acellular structure (A), enabling automated capture of high-resolution montage images for accurate lumen area assessment (B). Compaction of ASM spiderweb constructs followed a similar trajectory to ASM and CSM

652 sandwich constructs, being modulated by both time and stiffness (C; interaction $p=0.0036$, day $p<0.0001$,
653 stiffness $p=0.0036$, $n\geq16$). The contractile response was drug-dependent (D; interaction $p=0.7925$, drug
654 $p<0.0001$, stiffness $p=0.7656$, $n\geq5$); modest reductions in lumen area were observed after KCl, while
655 cytochalasin D completely reversed the contraction and enlarged lumen area above baseline levels. The
656 chelation-depolymerization load removal resulted in a dramatic reduction in lumen area (E; interaction
657 $p>0.9999$, time $p<0.0001$, stiffness $p=0.0126$, $n\geq3$), indicating that the muscle in ASM spiderwebs exerts
658 significant baseline tension, and that the spiderweb provides a strong elastic load that opposes the generated
659 forces. * represents a significant stiffness effect.

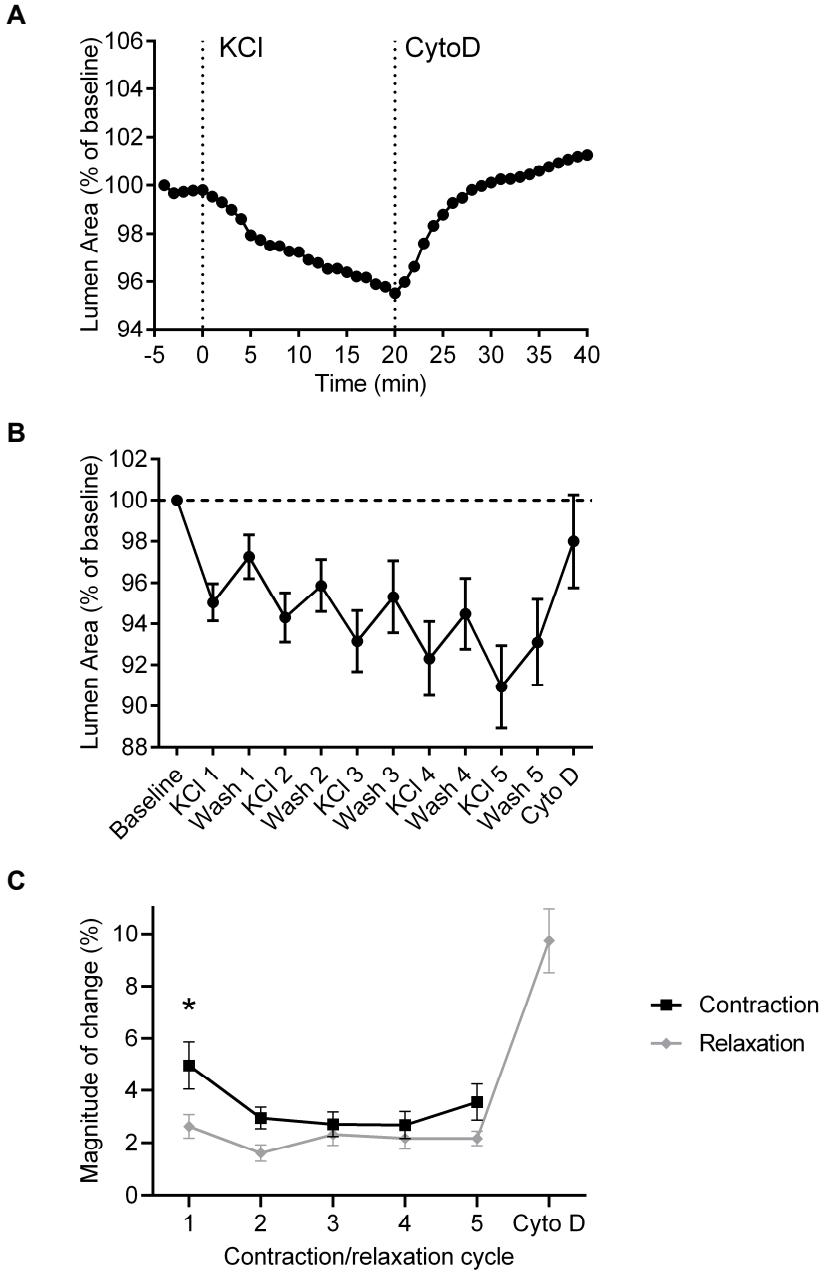

Figure 6. Dynamic properties of ASM spiderweb contractions.

Tracking a single contraction (A) reveals that a maximal dose of KCl results in a steady reduction in lumen area that does not peak after 20 minutes. Cytochalasin D results in lumen areas larger than baseline, entirely reversing the contraction plus highlighting baseline tone. Repeated contraction/relaxation cycles cause a progressive reduction in lumen area (B), resulting from each contraction being larger than the subsequent relaxation (C; interaction p=0.3465, cycle # p=0.0314, contract vs relax p=0.0005, n=10). Cytochalasin D can partly reverse the cumulative reduction in lumen area, indicating contributions from increasing muscle tension and plastic deformation of the construct. The final cytochalasin D treatment is shown for reference but is excluded from the statistical analysis. * represents a significant difference between contraction and relaxation.

669 **REFERENCES**

670

671 1. **Adams JC, Bell PD, Bodine SC, Brooks HL, Bunnett N, Joe B, Keehan KH, Kleyman TR, Marette A,**
672 **Morty RE, Ramirez JM, Thomsen MB, Yates BJ, and Zucker IH**. An American Physiological Society cross-journal
673 Call for Papers on "Deconstructing Organs: Single-Cell Analyses, Decellularized Organs, Organoids, and Organ-
674 on-a-Chip Models". *Am J Physiol Lung Cell Mol Physiol* 319: L266-L272, 2020.
675 2. **Huang D, Liu T, Liao J, Maharjan S, Xie X, Perez M, Anaya I, Wang S, Tirado Mayer A, Kang Z, Kong W,**
676 **Mainardi VL, Garciamendez-Mijares CE, Garcia Martinez G, Moretti M, Zhang W, Gu Z, Ghaemmaghami AM,**
677 **and Zhang YS**. Reversed-engineered human alveolar lung-on-a-chip model. *Proc Natl Acad Sci U S A* 118: 2021.
678 3. **Huh D, Matthews BD, Mammoto A, Montoya-Zavala M, Hsin HY, and Ingber DE**. Reconstituting organ-
679 level lung functions on a chip. *Science* 328: 1662-1668, 2010.
680 4. **Park JY, Ryu H, Lee B, Ha DH, Ahn M, Kim S, Kim JY, Jeon NL, and Cho DW**. Development of a
681 functional airway-on-a-chip by 3D cell printing. *Biofabrication* 11: 015002, 2018.
682 5. **Humayun M, Chow C-W, and Young EWK**. Microfluidic lung airway-on-a-chip with arrayable
683 suspended gels for studying epithelial and smooth muscle cell interactions. *Lab on a chip* 18: 1298-1309, 2018.
684 6. **Miller C, George S, and Niklason L**. Developing a tissue-engineered model of the human bronchiole. *J*
685 *Tissue Eng Regen Med* 4: 619-627, 2010.
686 7. **Chen YW, Huang SX, de Carvalho A, Ho SH, Islam MN, Volpi S, Notarangelo LD, Ciancanelli M,**
687 **Casanova JL, Bhattacharya J, Liang AF, Palermo LM, Porotto M, Moscona A, and Snoeck HW**. A three-
688 dimensional model of human lung development and disease from pluripotent stem cells. *Nat Cell Biol* 19: 542-
689 549, 2017.
690 8. **Tadokoro T, Wang Y, Barak LS, Bai Y, Randell SH, and Hogan BL**. IL-6/STAT3 promotes regeneration of
691 airway ciliated cells from basal stem cells. *Proc Natl Acad Sci U S A* 111: E3641-3649, 2014.
692 9. **Boecking CA, Walentek P, Zlock LT, Sun DI, Wolters PJ, Ishikawa H, Jin BJ, Haggie PM, Marshall WF,**
693 **Verkman AS, and Finkbeiner WE**. A simple method to generate human airway epithelial organoids with
694 externally orientated apical membranes. *Am J Physiol Lung Cell Mol Physiol* 322: L420-L437, 2022.
695 10. **van Riet S, van Schadewijk A, Khedoe P, Limpens R, Barcena M, Stolk J, Hiemstra PS, and van der**
696 **Does AM**. Organoid-based expansion of patient-derived primary alveolar type 2 cells for establishment of
697 alveolus epithelial Lung-Chip cultures. *Am J Physiol Lung Cell Mol Physiol* 322: L526-L538, 2022.
698 11. **Tliba O, Amrani Y, and Panettieri RA, Jr.** Is airway smooth muscle the "missing link" modulating airway
699 inflammation in asthma? *Chest* 133: 236-242, 2008.
700 12. **Cooper PR, McParland BE, Mitchell HW, Noble PB, Politi AZ, Ressmeyer AR, and West AR**. Airway
701 mechanics and methods used to visualize smooth muscle dynamics in vitro. *Pulm Pharmacol Ther* 22: 398-406,
702 2009.

703 13. **Wright D, Sharma P, Ryu MH, Risse PA, Ngo M, Maarsingh H, Koziol-White C, Jha A, Halayko AJ, and**
704 **West AR**. Models to study airway smooth muscle contraction in vivo, ex vivo and in vitro: implications in
705 understanding asthma. *Pulm Pharmacol Ther* 26: 24-36, 2013.
706 14. **Noble PB, Pascoe CD, Lan B, Ito S, Kistemaker LE, Tatler AL, Pera T, Brook BS, Gosens R, and West AR**.
707 Airway smooth muscle in asthma: linking contraction and mechanotransduction to disease pathogenesis and
708 remodelling. *Pulm Pharmacol Ther* 29: 96-107, 2014.
709 15. **Ceresa CC, Knox AJ, and Johnson SR**. Use of a three-dimensional cell culture model to study airway
710 smooth muscle-mast cell interactions in airway remodeling. *Am J Physiol Lung Cell Mol Physiol* 296: L1059-
711 1066, 2009.
712 16. **Long X, Bell RD, Gerthoffer WT, Zlokovic BV, and Miano JM**. Myocardin is sufficient for a smooth
713 muscle-like contractile phenotype. *Arterioscler Thromb Vasc Biol* 28: 1505-1510, 2008.
714 17. **Matsumoto H, Moir LM, Oliver BG, Burgess JK, Roth M, Black JL, and McParland BE**. Comparison of
715 gel contraction mediated by airway smooth muscle cells from patients with and without asthma. *Thorax* 62:
716 848-854, 2007.
717 18. **West AR, Zaman N, Cole DJ, Walker MJ, Legant WR, Boudou T, Chen CS, Favreau JT, Gaudette GR,**
718 **Cowley EA, and Maksym GN**. Development and characterization of a 3D multicell microtissue culture model of
719 airway smooth muscle. *Am J Physiol Lung Cell Mol Physiol* 304: L4-16, 2013.
720 19. **Nesmith AP, Agarwal A, McCain ML, and Parker KK**. Human airway musculature on a chip: an in vitro
721 model of allergic asthmatic bronchoconstriction and bronchodilation. *Lab on a chip* 14: 3925-3936, 2014.
722 20. **Morris GE, Bridge JC, Eltboli OM, Lewis MP, Knox AJ, Aylott JW, Brightling CE, Ghaemmaghami AM,**
723 **and Rose FR**. Human airway smooth muscle maintain in situ cell orientation and phenotype when cultured on
724 aligned electrospun scaffolds. *Am J Physiol Lung Cell Mol Physiol* 307: L38-47, 2014.
725 21. **Dickman CTD, Russo V, Thain K, Pan S, Beyer ST, Walus K, Getsios S, Mohamed T, and Wadsworth SJ**.
726 Functional characterization of 3D contractile smooth muscle tissues generated using a unique microfluidic 3D
727 bioprinting technology. *FASEB J* 34: 1652-1664, 2020.
728 22. **Zhang J, Wehrle E, Vetsch JR, Paul GR, Rubert M, and Muller R**. Alginate dependent changes of
729 physical properties in 3D bioprinted cell-laden porous scaffolds affect cell viability and cell morphology. *Biomed*
730 *Mater* 14: 065009, 2019.
731 23. **Shi P, Laude A, and Yeong WY**. Investigation of cell viability and morphology in 3D bio-printed alginate
732 constructs with tunable stiffness. *Journal of biomedical materials research Part A* 105: 1009-1018, 2017.
733 24. **Cheng D, Jiang C, Xu J, Liu Z, and Mao X**. Characteristics and applications of alginate lyases: A review.
734 *Int J Biol Macromol* 164: 1304-1320, 2020.
735 25. **Lueckgen A, Garske DS, Ellinghaus A, Mooney DJ, Duda GN, and Cipitria A**. Enzymatically-degradable
736 alginate hydrogels promote cell spreading and in vivo tissue infiltration. *Biomaterials* 217: 119294, 2019.

737 26. **Wu Z, Su X, Xu Y, Kong B, Sun W, and Mi S**. Bioprinting three-dimensional cell-laden tissue constructs
738 with controllable degradation. *Sci Rep* 6: 24474, 2016.
739 27. **Iskandar L, Rojo L, Di Silvio L, and Deb S**. The effect of chelation of sodium alginate with osteogenic
740 ions, calcium, zinc, and strontium. *J Biomater Appl* 34: 573-584, 2019.
741 28. **Chin LY, Bosse Y, Jiao Y, Solomon D, Hackett TL, Pare PD, and Seow CY**. Human airway smooth muscle
742 is structurally and mechanically similar to that of other species. *Eur Respir J* 36: 170-177, 2010.
743 29. **Panitch HB, Deoras KS, Wolfson MR, and Shaffer TH**. Maturational changes in airway smooth muscle
744 structure-function relationships. *Pediatr Res* 31: 151-156, 1992.
745 30. **Jamieson RR, Stasiak SE, Polio SR, Augspurg RD, McCormick CA, Ruberti JW, and Parameswaran H**.
746 Stiffening of the extracellular matrix is a sufficient condition for airway hyperreactivity. *J Appl Physiol (1985)*
747 130: 1635-1645, 2021.
748 31. **Nizamoglu M, de Hilster RHJ, Zhao F, Sharma PK, Borghuis T, Harmsen MC, and Burgess JK**. An in vitro
749 model of fibrosis using crosslinked native extracellular matrix-derived hydrogels to modulate biomechanics
750 without changing composition. *Acta biomaterialia* 147: 50-62, 2022.
751 32. **Lai VK, Frey CR, Kerandi AM, Lake SP, Tranquillo RT, and Barocas VH**. Microstructural and mechanical
752 differences between digested collagen-fibrin co-gels and pure collagen and fibrin gels. *Acta biomaterialia* 8:
753 4031-4042, 2012.
754 33. **Araujo BB, Dolhnikoff M, Silva LF, Elliot J, Lindeman JH, Ferreira DS, Mulder A, Gomes HA, Fernezlian**
755 **SM, James A, and Mauad T**. Extracellular matrix components and regulators in the airway smooth muscle in
756 asthma. *Eur Respir J* 32: 61-69, 2008.
757 34. **Elshaw SR, Henderson N, Knox AJ, Watson SA, Buttle DJ, and Johnson SR**. Matrix metalloproteinase
758 expression and activity in human airway smooth muscle cells. *Br J Pharmacol* 142: 1318-1324, 2004.
759 35. **Jablonska-Trypuc A, Matejczyk M, and Rosochacki S**. Matrix metalloproteinases (MMPs), the main
760 extracellular matrix (ECM) enzymes in collagen degradation, as a target for anticancer drugs. *J Enzyme Inhib*
761 *Med Chem* 31: 177-183, 2016.
762 36. **Shin YJ, Shafranek RT, Tsui JH, Walcott J, Nelson A, and Kim DH**. 3D bioprinting of mechanically tuned
763 bioinks derived from cardiac decellularized extracellular matrix. *Acta biomaterialia* 119: 75-88, 2021.
764 37. **De Santis MM, Alsafadi HN, Tas S, Bolukbas DA, Prithiviraj S, Da Silva IAN, Mittendorfer M, Ota C,**
765 **Stegmayr J, Daoud F, Konigshoff M, Sward K, Wood JA, Tassieri M, Bourgine PE, Lindstedt S, Mohlin S, and**
766 **Wagner DE**. Extracellular-Matrix-Reinforced Bioinks for 3D Bioprinting Human Tissue. *Adv Mater* 33: e2005476,
767 2021.
768